This is a pre print version of the following article:

Single MoS2 Nanotube Experimental Optical Extinction Cross Section / Colosimo, A., Crut, A., Lascoux, N., Panais, C., Casto, A., Vialla, F., Demontis, V., Martini, L., Rosi, P., Rotunno, E., Gazzadi, G.C., Beleggia, M., Krishnappa, M., Zak, A., Beltram, F., Rossella, F., Vallee, F., Del Fatti, N., Banfi, F., Maioli, P.. - In: JOURNAL OF PHYSICAL CHEMISTRY. C. - ISSN 1932-7447. - 129:10(2025), pp. 5086-5094. [10.1021/acs.jpcc.4c08613]

Terms of use:

The terms and conditions for the reuse of this version of the manuscript are specified in the publishing policy. For all terms of use and more information see the publisher's website.

07/11/2026 20:17

(Article begins on next page)

Single MoS2 Nanotube Experimental Optical Extinction Cross Section

Alessia Colosimo, Clément Panais, Aurélien Crut, Noëlle Lascoux, Alessandro Casto, Fabien Vialla, Valeria Demontis, Leonardo Martini, Paolo Rosi, Enzo Rotunno, et al.

▶ **To cite this version:**

Alessia Colosimo, Clément Panais, Aurélien Crut, Noëlle Lascoux, Alessandro Casto, et al.. Single MoS2 Nanotube Experimental Optical Extinction Cross Section. Journal of Physical Chemistry C, 2025, 129 (10), pp.5086-5094. 10.1021/acs.jpcc.4c08613 . hal-05002311

HAL Id: hal-05002311
https://hal.science/hal-05002311v1

Submitted on 23 Mar 2025

HAL is a multi-disciplinary open access archive for the deposit and dissemination of scientific research documents, whether they are published or not. The documents may come from teaching and research institutions in France or abroad, or from public or private research centers.

L'archive ouverte pluridisciplinaire **HAL**, est destinée au dépôt et à la diffusion de documents scientifiques de niveau recherche, publiés ou non, émanant des établissements d'enseignement et de recherche français ou étrangers, des laboratoires publics ou privés.

Distributed under a Creative Commons CC BY 4.0 - Attribution - International License

Single MoS_2 Nanotube experimental optical extinction cross section

Alessia Colosimo,[†,‡] Aurélien Crut,[†] Nöelle Lascoux,[†] Clément Panais,[†] Alessandro Casto,[†] Fabien Vialla,[†] Valeria Demontis,[¶] Leonardo Martini,[§] Paolo Rosi,[§] Enzo Rotunno,[‖] Giancarlo Gazzadi,[‖] Marco Beleggia,[§] Manjunath Krishnappa,[⊥,#] Alla Zak,[⊥] Fabio Beltram,[@] Francesco Rossella,[§] Fabrice Vallée,[†] Natalia Del Fatti,[*,†,△] Francesco Banfi,[*,†] and Paolo Maioli[†]

†*Université Claude Bernard Lyon1, CNRS, Institut Lumière Matière, F-69622 Villeurbanne, France*

‡*NEST, Scuola Normale Superiore, Piazza S. Silvestro 12, I-56124 Pisa, Italy*

¶*Dipartimento di Fisica, Università degli Studi di Cagliari, Cittadella Universitaria di Monserrato, S.P. 8 km 0,700 - 09042 Monserrato (CA)*

§*Dipartimento di Scienze Fisiche, Informatiche e Matematiche, University of Modena and Reggio Emilia, via Campi 213/a, I-41125 Modena, Italy*

‖*S3, Istituto Nanoscienze-CNR, via Campi 213/a, I-41125 Modena, Italy*

⊥*Department of Physics, HIT- Holon Institute of Technology, 52 Golomb St., Holon 5810201, Israel*

#*Dept. of Chemistry, Nitte Meenakshi Institute of Technology, Bangalore-560064, Karnataka, India*

@*NEST, Scuola Normale Superiore and Istituto Nanoscienze-CNR, Piazza S. Silvestro 12, I-56124 Pisa, Italy*

△*Institut Universitaire de France (IUF), France*

E-mail: natalia.del-fatti@univ-lyon1.fr; francesco.banfi@univ-lyon1.fr

Abstract

The experimentally retrieved value of the optical extinction cross section per unit length, $\sigma_{L,ext}^{NT}$, of individual MoS_2 multi-wall nanotubes is here reported over the 440 - 940 nm wavelength range, for light polarization both parallel and perpendicular to the nanotube longitudinal axis. The impact of nanotube diameter and environment on $\sigma_{L,ext}^{NT}$ is addressed for individual nanotubes with diameters of 120 and 220 nm, in suspended, sapphire-supported, and PMMA-supported configurations. Measuring on individual nanotubes is of the utmost importance given the wide nanotube size dispersion intrinsic to the synthesis process. The findings are interpreted in conjunction with finite element method simulations, informed by morphological input parameters from electron microscopies, offering insight into the respective contributions of absorption and scattering cross sections per unit length to the overall $\sigma_{L,ext}^{NT}$. These quantitative results are of relevance in view of optoelectronics applications involving MoS_2 nanotubes, while providing benchmark values for theoretical investigations on their nanooptical response.

Introduction

Recently, transition-metal dichalcogenides nanotubes (NTs) have been sparking widespread

research interest.[1,2] Their multi-wall structure, once considered a limitation, has proven to be a unique advantage, yielding intriguing discoveries and numerous applications.[3–5] Significantly, the relatively novel MoS_2 NTs have demonstrated noteworthy optoelectronic properties,[6–8] encompassing exciton coupling with cavity modes in large-radius multi-walled NTs,[9–12] in addition to nonlinear optical properties.[13] Notwithstanding its importance, the optical extinction cross section per unit length, $\sigma^{NT}_{L,ext}$ $[nm^2/nm]$, which governs the attenuation of an optical beam upon interaction with a MoS_2 NT, remains unresolved. Indeed, MoS_2 multiwall NTs synthesis has long been a challenging and puzzling process.[1,2,14–16] Only recently a reliable method for producing samples with pure phases has been developed.[16] However, the method still results in a wide dispersion of NTs sizes and morphologies, thus calling for measurements on individual NTs.[11]

In this work, we provide the first quantitative measurements of the optical *extinction* cross section per unit length, $\sigma^{NT}_{L,ext}$, for *single* MoS_2 multi-wall NTs, examining the spectral response across the 440-940 nm range, for light polarization both parallel and perpendicular to the NT longitudinal axis. The impact of the diameter of the NT (∼120 nm and ∼220 nm) and its surroundings on $\sigma^{NT}_{L,ext}$ is examined by measuring individual NTs in three distinct configurations: suspended, supported on PMMA, and on sapphire. These configurations are paradigmatic for the case of isolated, and wide-band-gap insulator and polymer-supported NT, respectively. Finite element simulations are performed upon insertion of morphological input parameters from electron microscopies acquired on the NTs that were optically measured. Simulations provide indications on the relative contribution of *absorption*, $\sigma^{NT}_{L,abs}$, and *scattering*, $\sigma^{NT}_{L,sca}$, cross section per unit length to $\sigma^{NT}_{L,ext} = \sigma^{NT}_{L,abs} + \sigma^{NT}_{L,sca}$.

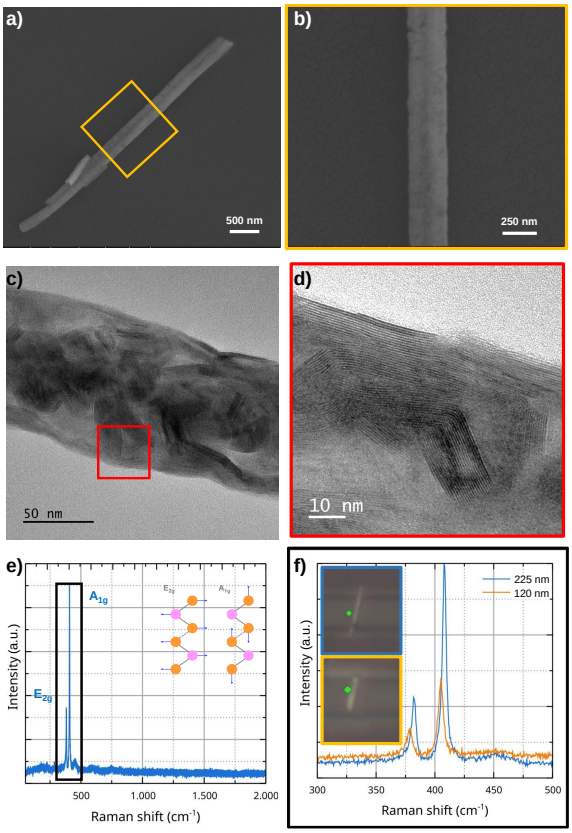

Figure 1: Structural and morphological characterization. a) SEM micrograph of a measured individual MoS_2 NT after metallization and displacement onto a SiO_2/Si substrate (for high resolution imaging). b) High magnification detail of the central section of the nanostructure shown in panel a. c) TEM micrograph of one of the investigated NTs and (d) high resolution TEM micrograph of a section of the same nanostructure: multi-layered grains with different layer orientation are visible. e) Representative Raman spectrum acquired on a suspended NT: the two main peaks of MoS_2 are clearly visible, while there is no sign of spurious molybdenum oxide peaks. f) Raman spectra of two NTs with different diameters (inset: optical images).

Methods

MoS_2 NTs Synthesis. Highly crystalline multiwalled MoS_2 NTs are synthesized in a horizontal reactor equipped with a porous-quartz reaction cell and a split furnace whose temperature profile is controlled with ±2 °C precision. The process involves multiple steps, each carried out within the same reactor but at different temperatures and flow conditions of reactive gases. Initially, the temperature is increased to 550-620 °C and the N_2 carrier gas is injected into the reactor for 30 minutes to

obtain an inert atmosphere. Afterwards, the reactive gases (H_2 or/and H_2S) and carrier N_2 gas are injected with the flow rates depending on the reaction step and regulated by electronic mass flow controllers (MFC). The MoO_3 precursor powder in the porous quartz cell is inserted in the hot zone and the growth of suboxide nanowhiskers - intermediate precursors for NTs - starts. The growth follows a few steps: evaporation of MoO_3 powder into 3-5 molecular clusters, their partial reduction into MoO_2 and following "chemical condensation" of MoO_3 and MoO_2 vapors into suboxide Mo_4O_{11} nanowhiskers, while non-volatile MoO_2 serves as a center of crystallization. When the first stage of oxide nanowhiskers growth is completed, the reaction cell is removed from the hot zone and the temperature of the furnace is raised for the next reaction steps. A second stage is dedicated to the conversion of suboxide nanowhiskers into MoS_2 NTs. When the 600-620 °C temperature and reactor inert atmosphere are obtained, the H_2S gas is injected, to trigger the sulfurization reaction. The oxide-to-sulfide conversion starts from the nanowhiskers' surface. Once external walls are grown and the 1D structure becomes stable, the temperature is increased to 800 °C and the reaction proceeds inward until all the oxide is converted to molybdenum sulfide NTs with highly crystalline layered walls. As a result of the difference in the compounds' densities, this process leads to the formation of hollow MoS_2 NTs. A detailed description of this process was reported earlier.[16]

Nanofabrication. The fabrication protocol allows to suspend individual nanostructures over trenches defined in the deposition substrate, the latter being made of a material that is transparent within the wavelength range of interest: 440-940 nm. This allows us to investigate the NTs with an optical setup operating in transmission mode. A 10 x 10 mm^2 sapphire substrate, 0.48 mm thick, was used. Electron Beam Lithography (EBL), metal (5/50nm Ti/Au) evaporation and lift-off process were exploited to realize markers on the substrate, that are essential for identifying specific individual NTs and for precisely locating them when the sample is placed in the optical setup. A second lithography step allows to define and then etch micrometric width trenches into a 300 nm-thick layer of a positive resist based on polymethyl methacrylate (PMMA). After baking the substrate coated with the PMMA, we drop-cast NTs, previously diluted in ethanol, onto the surface at a concentration that ensures a spatial separation of approximately 10 μm between adjacent nanostructures. Upon drop-casting, optical and electron microscopies reveal the occurrence of NTs suspended over the trenches, NTs laying on the PMMA layer (within two trenches) and NTs laying on the sapphire substrate (on a trench bottom).

Electron microscopies. The Scanning Electron Microscope (SEM) images of the NTs are obtained with a FEI Quanta-200 system. All the images are captured via the secondary electron detector and electron beam acceleration of 15.0 kV. For high-resolution images, and after optical spectroscopy has been performed, the measured NTs are metallized and displaced onto a SiO_2/Si substrate. The structural characterization of MoS_2 NTs is conducted using high-resolution transmission electron microscopy (HRTEM). The imaging is performed on a ThermoFisher Talos FS200 microscope, equipped with a Schottky field emission gun (FEG), operating at an accelerating voltage of 200 kV. The sample is prepared by displacing the NTs onto holey carbon-coated copper TEM grids, ensuring minimal overlap between the structures and sufficient transparency for electron imaging. Imaging is performed at different magnifications to capture different aspects of the NT morphology, with particular attention to the number and arrangement of the layers in both the pristine and defective regions. High-resolution images are acquired at low electron dose rates to minimize beam-induced damage, which is especially critical for nanostructures like MoS_2 that are sensitive to prolonged electron exposure.

μ-Raman. Raman spectroscopy is performed on the investigated NTs using a Horiba LabRAM HR Evolution micro-spectrometer equipped with a solid-state laser centered at 532 nm (max power 100 mW). We use a diffraction grating with 1800 G/mm in the single spectra.

Single spectra are recorded on the sample, using a 100X magnification lens that provides a Gaussian beam focused on the surface with FWHM $\sim$1.5 μm and energy intensity of 0,63 mJ/μm^2 over an acquisition time of 5 s with 3 accumulations to reduce noise. The extended spectrum is automatically generated by the Horiba acquisition software, merging 4 consecutive spectra acquired with different Raman shift range.

Optical spectroscopy. The extinction cross section per unit length of MoS_2 NTs, $\sigma^{NT}_{L,ext}$, is measured using extinction spectroscopy in a setup equipped with a tunable Ti:Sa femtosecond laser source (Chameleon Ultra II). The wavelength is extended to encompass the range 440-940 nm by an automated Optical Parametric Oscillator (OPO) (Chameleon Compact OPO-Vis) in conjunction with second harmonic generation. Two Apochromatic 100X magnification objectives with 0.7 numerical aperture (N.A.) are used to focus light onto the sample (input objective) and collect the transmitted signal (output objective). The sample holder is connected to a piezoelectric controller, allowing for raster-scan operations. The 2D spatial map of the light transmitted through the nano-object is acquired via Lock-In detection (see SI for setup details). A post-processing analysis of the map, developed in the discussion section, ultimately allows retrieval of $\sigma^{NT}_{L,ext}$.

Simulations. Simulations of the optical cross sections is performed with input data from morphological characterization and running tables of refraction indexes available in the literature. Numerical models are implemented and solved via Finite Element Modeling (FEM). Refer to SI for further details.

Results and discussion

Structure and morphology. A combined SEM and TEM investigation was carried out on individual NTs from the same growth batch deposited by drop-casting onto different substrates (SiO_2/Si for SEM, or TEM grids), revealing the occurrence of two main populations of NTs displaying average diameters of 120 nm (small NTs) and 220 nm (large NTs). The same investigation was then repeated on the NTs on which optical spectroscopy was performed. Specifically, Figure 1a shows the SEM micrograph of a large NT laying onto the SiO_2/Si substrate. The image was taken after measuring $\sigma^{NT}_{L,ext}$ of the very same NT originally suspended on the PMMA trench, see Figure 2b. The nanostructure is 4.3 μm long and displays a diameter that varies between the two ends of the NT. However, the high-resolution imaging of the central section of the NT (the section relevant for extraction of $\sigma^{NT}_{L,ext}$), shown in Figure 1b, indicates a diameter of 225 $\pm$ 8 nm.

For the smaller NTs, with diameters in the order of 120 nm, an extensive TEM study was performed. Figure 1c shows the TEM micrograph of one of the investigated nanostructures. This allows to precisely measure the diameter change along the axial direction, indicating a diameter in the range 116-127 nm. The NT exhibits the characteristic layered structure, with multiple walls consisting of MoS_2 layers. Such multiwalled structure appears inhomogeneous1c and d, with layers occasionally terminating either on the outer surface or within the wall. This phenomenon, very common in layered van der Waals materials, occurs when layers within the NT terminate in a dislocation-like fashion, disrupting the regular stacking of MoS_2 layers. However, rather than an almost perfectly-ordered crystalline structure with a few evident layer terminations, the NTs exhibit noticeable internal contrast variations, which may indicate some structural irregularities or a degree of inhomogeneity in the layering. This suggests the occurrence of several multiwalled domains with different orientations of the MoS_2 layers. This scenario was verified by taking high resolution TEM micrographs of selected areas of the nanostructures, allowing to clearly identify single multi-layered domains of MoS_2. Figure 1d shows a defective region of the external region of the NT, where the MoS_2 layers are visibly disordered. These defects may be related to buckling instabilities or internal stresses that arise as the NT diameter increases, complicating the regular arrangement of layers. Similar considerations hold for the wide diameter sample.

We used Raman spectroscopy to investigate the structural properties of the measured individual NTs. The main Raman peaks displayed by the nanostructures are the E_{2g}, that represents in-plane vibrations of MoS_2 molecules and is centered at 380 cm^{-1} and the A_{1g}, that represents out-of-plane vibrations of MoS_2 molecules and is peaked at 410 cm^{-1}.[17] As an example, in Figure 1e we report an extended spectrum measured at a suspended NT site, where the two typical peaks of MoS_2 are present. Importantly, the absence of satellite peaks at 280 cm^{-1} and 816 cm^{-1}, usually attributed to MoO_x crystal phases,[18] indicates the excellent purity of the material. Figure 1f reports the Raman spectra measured in two NTs with different cross sections. Both E_{2g} and A_{1g} peaks blue-shift passing from the smaller to the larger NT. In particular, the E_{2g} (A_{1g}) mode is centered at 378 (405) cm^{-1} in the smaller NT and at 382 (408) cm^{-1} in the larger. In the layered MoS_2 planar system, the energy distance between the two peaks is correlated to the number of layers[17] and the presence of defects.[19,20] Extrapolating to our case, the observed distance of 27 (26) cm^{-1} in the smaller (larger) NTs is fully compatible with a multiwalled structure with 10 or more walls of MoS_2.

Retrieval of $\sigma^{NT}_{L,ext}$: concept. To outline the retrieval method, we consider the case reported in Figure 2a. The Gaussian laser beam, full width half maximum ($FWHM$) d and wavelength λ, is focused on a single NT via the input objective, the optical input power on the sample being P_{in}. The center of the laser spot (which is kept fixed in the same position) defines the origin of the coordinate system illustrated in Figure 2a bottom panel, where the x and y axes are taken along the NT longitudinal axis and perpendicular to it, respectively. The NT, whose center C has coordinate (x_C, y_C), is scanned via a translation stage across the entire waist of the laser beam, i.e. starting from $y_C = -\infty$ (actually $y_C \ll -d$) to $y_C = +\infty$ (actually $y_C \gg +d$) while keeping x_C constant. For each position y_C of the NT, the transmitted light is collected through the output objective and fed to a photodetector. With reference to Figure 2a top panel, $P_{out}(y_C)$ indicates the collected optical power. $P_{out}(\infty)$ is then the power collected after transmission throughout the sapphire substrate only, that is, when the NT is completely outside the laser beam.

We now relate the output optical power to the power extinction caused by the presence of the *suspended* NT (i.e. NT and the air gap between NT and the sapphire substrate) and the substrate. The power extinction, for the case of the laser beam impinging on the substrate alone (with the NT translated out of the beam), is $P_{out}(\infty) = T_{sub}P_{in}$, with T_{sub} the power transmission coefficient. The power extinction adding the NT is then cast in the form:

$$P_{out}(y_C) = T_{sub}\left(P_{in} - P^{NT}_{ext}(y_C)\right) \qquad (1)$$

The present formulation, accounting for the cascade of power losses, allows one to define the NT extinction cross section. Within the present approach, coherence effects are encapsulated in $P^{NT}_{ext}(y_C)$. This is achieved by taking $P_{out}(y_C)$ as the measured quantity and using Equation 1, which then serves as the definition of $P^{NT}_{ext}(y_C)$.

Equation 1 is conveniently cast in the form:

$$P_{out}(y_C) = P_{out}(\infty) \times \left(1 - \frac{P^{NT}_{ext}(y_C)}{P_{in}}\right) \qquad (2)$$

For the textbook case of an infinitely extended plane wave with spatially constant fluence, I_{in}, impinging on the NT, one would have $P^{NT}_{ext} = \sigma^{NT}_{ext} \times I_{in}$, with σ^{NT}_{ext} $[nm^2]$ the NT extinction cross section. For the present case of a Gaussian laser beam the fluence reads $I_{in}(x,y) = \frac{P_{in}}{2\pi s^2} \times exp(-\frac{x^2+y^2}{2s^2})$, with $s = d/(2\sqrt{2ln2})$ the standard deviation, yielding:

$$P^{NT}_{ext}(y_C) = \sigma^{NT}_{A,ext} \times \int_{-\frac{L}{2}}^{+\frac{L}{2}} \int_{y_C-\frac{D}{2}}^{y_C+\frac{D}{2}} I_{in}(x,y)\,dxdy \qquad (3)$$

where $\sigma^{NT}_{A,ext}$ $[nm^2/nm^2]$ defines the NT extinction-cross section *per unit area*. Inser-

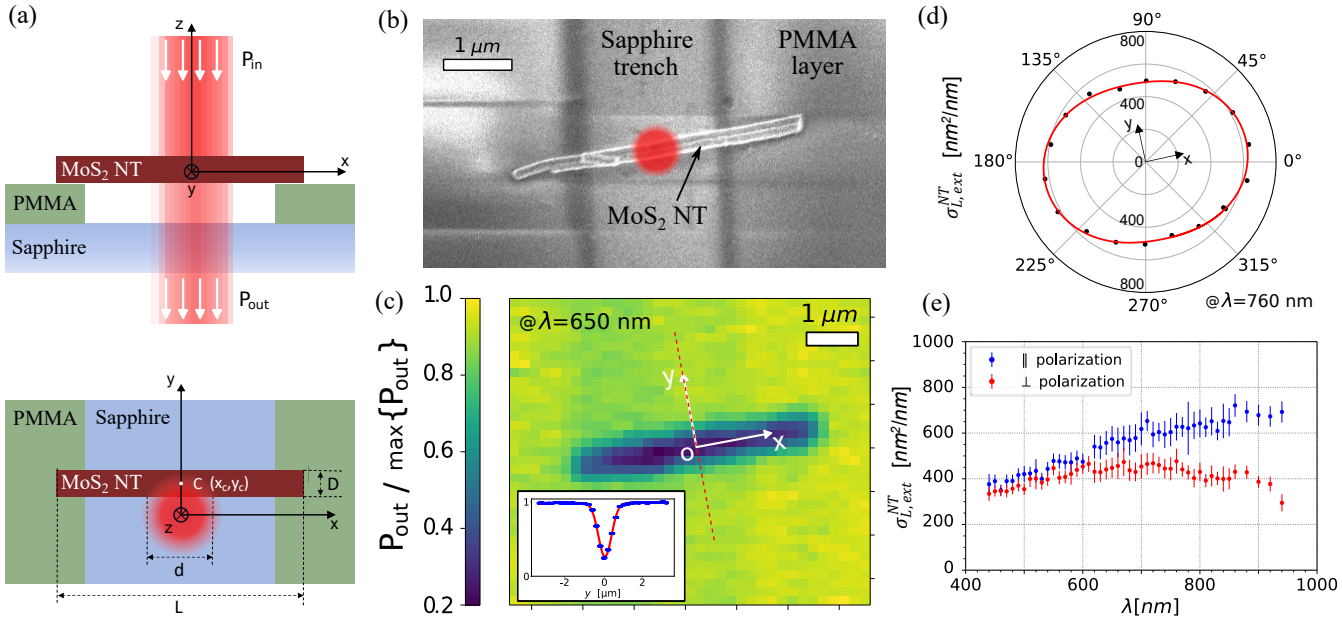

Figure 2: Retrieval of $\sigma^{NT}_{L,ext}$. Illustrations for a suspended NT, D=225 nm.
Panel (a): schematics of the measurement principle. Top panel: side view. Bottom panel: top view. The laser Gaussian beam (red) is kept fixed over the sample. The origin of the coordinate axis, O, is taken at the beam center. P_{in} and P_{out} are the input and output (collected) optical power, respectively. C is the center of the NT of coordinates (x_C,y_C). The NT is swept across the laser beam along the y-axis, i.e. keeping x_C=0. Panel (b) MoS_2 NT, D=225 nm, L=4.3 μm, suspended over a sapphire trench 2 μm wide and 300 nm deep. Red circle: schematics of the laser beam of FWHM d=650 nm. Panel (c): $P_{out}/max\{P_{out}\}$ colormap obtained at λ=650 nm, polarization parallel to the NT longitudinal axis, scanning a 7 μm×7μm area with the NT. The superposed coordinate axis matches the one in panel (a). Red dashed line: cut passing through the center of the nanotube and orthogonal to its longitudinal axis yielding $P_{out}(x_C = 0, y_C)/max\{P_{out}\}$. Inset: $P_{out}(x_C = 0, y_C)/max\{P_{out}\}$ data points (blue dots) acquired along the red dashed line and fit (continuous red line) to Equation 4 normalized to $max\{P_{out}\}$. Panel (d): polar plot of $\sigma^{NT}_{L,ext}$ for λ=760 nm (black dots) together with its angular fit (red line). Panel (e): $\sigma^{NT}_{L,ext}$ vs λ for laser polarization parallel (blue) and perpendicular (red) to the NT longitudinal axis.

tion of Equation 3 into Equation 2 yields:

$$P_{out}(y_C) = P_{out}(\infty)\left\{1 - \sigma^{NT}_{A,ext} \times \frac{1}{2} erf\left(\sqrt{ln2}\frac{L}{d}\right) \times \left[erf\left(\sqrt{ln2}\frac{(2y_C + D)}{d}\right) - erf\left(\sqrt{ln2}\frac{(2y_C - D)}{d}\right)\right]\right\} \quad (4)$$

D and L are known from morphological characterization, leaving d and $\sigma^{NT}_{A,ext}$ as the sole free parameters. Fitting the experimental curve $P_{out}(y_C)$ with Equation 4 therefore allows us to retrieve $\sigma^{NT}_{A,ext}$ (together with d). In our experiment $L > d$. The fact that the value of L is a few times that of d, renders $erf(\sqrt{ln2}L/d) \sim 1$. This makes the fit function Equation 4 effectively independent of L. The cross section *per unit length*, $\sigma^{NT}_{L,ext}$=$D \times \sigma^{NT}_{A,ext}$ [nm^2/nm], then becomes the relevant quantity to be addressed and will be the focus of our analysis for the remainder of this discussion. We note that, in retrieving $\sigma^{NT}_{L,ext}$ from the previous analysis, i.e. Equation 2, we do not take into account the portion of the scattered field that falls within the collecting objective's acceptance angle.[21] This approximation may result in a reduced extinction cross section, slightly inferior as compared to the full extinction case.

Retrieval of $\sigma_{L,ext}^{NT}$: experiment. We now adapt the conceptual framework outlined above to the actual experiment. We discuss the case of the NT shown in the SEM image in Figure 2b. In experiments, the NT is not exactly arranged perpendicular to the PMMA ridges. Furthermore, once the chip is mounted under the input objective, the NT longitudinal axis is commonly not perpendicular to the translation-stage axis movement. To overcome these limitations, we proceed as follows.

We first mount the chip under the input objective and focus the laser beam on the NT plane. We then raster scan the NT across a $7\mu m \times 7\mu m$ area, acquiring P_{out} at each position. The scan area linear dimensions far exceed the laser $FWHM$. The measurement is performed exploiting lock-in detection. Furthermore, to remedy for possible laser fluctuations, a portion of the incoming laser beam is fed to a reference photodiode before entering the input objective, see Figure S1 for a detailed setup. Figure 2c shows the spatial distribution of P_{out}, normalized to its peak value, obtained by raster-scanning the NT reported in Figure 2b, diameter D = 225 nm and length L = 4.2 μm, across a laser beam with wavelength λ = 650 nm, d=650 nm and polarization parallel to the NT longitudinal axis.

A cigar-like blue shape is clearly visible in the colormap. When the center C of the NT is moved to coincide with the center of the laser beam O, the most intense portion of the beam is attenuated by the NT, hence yielding the minimum value of P_{out}, i.e. occurring at the center of the cigar-like blue shape. We note that the contour of the cigar-like blue shape does not exactly represent the NT shape. It would only be so if the NT dimensions were greatly exceeding d. This is certainly not the case here for the NT transversal dimension where $d \sim 2.5D$, see SI on this point.

The center O of the Gaussian laser beam and the NT longitudinal axis are identified in Figure 2c. We then superpose the same coordinate axis defined in Figure 2a, allowing us to recover the correct reference frame for Equation 4. Taking a cut of the colormap data along the y axis (see the red dashed line on the colormap) thus yields $P_{out}(y_C)$ normalized to $max\{P_{out}\}$, see dotted data points in inset to 2c. The latter trace is then fitted to Equation 4 upon proper normalization, see continuous red line in inset to 2c, ultimately yielding $\sigma_{L,ext}^{NT}$. The latter quantity has a marked dependence on the beam polarization: Figure 2d reports $\sigma_{L,ext}^{NT}$ as a function of the polarization angle taken for λ=760 nm. The coordinate axis superposed on the polar plot is the same as in panel (c), i.e. the x axis identifying the NT longitudinal axis. The values span from a maximum of 628 nm^2/nm to a minimum of 477 nm^2/nm for longitudinal and perpendicular (with respect to the NT axis) polarization, respectively. The measurement is repeated varying λ in the 440-940 nm range and for light polarization both parallel and perpendicular to the NT longitudinal axis, yielding the plot in Figure 2e.

Experimental assessment of $\sigma_{L,ext}^{NT}$. The measured values $\sigma_{L,ext}^{NT}$ vs λ are reported in Figure 3 for both parallel (blue dots) and perpendicular (red dots) polarizations. Graphs in the first row (panels a-c) pertain to small diameter NTs, $D \sim$ 120 nm, whereas the second row (panels e-g) shows data for wide diameter NTs, $D \sim$ 225 nm. The first column (panels a and d) pertains to the suspended NT case, the second (panels b and e) and the third (panels c and f) to the PMMA and sapphire-supported NT, respectively. These are the first available values for the MoS_2 *absolute* extinction cross section, setting $\sigma_{L,ext}^{NT}$ in the tens to few hundreds of nm^2/nm range, depending on wavelength, size, environment and polarization.

Small diameters: D∼120 nm case. $\sigma_{L,ext}^{NT}$ is greater for the suspended NT, as compared to the substrate-supported cases, over the entire wavelength range for both polarizations, despite having a slightly smaller diameter than the sapphire-supported NT. For parallel polarization, $\sigma_{L,ext}^{NT}$ for the suspended NT exceeds by a factor of $\sim$ two those of the substrate-supported cases in the low- and high-wavelength region. The values for the PMMA and sapphire supported NT are within the same range up to λ = 750 nm. The $\sigma_{L,ext}^{NT}$ for the PMMA-supported NT exceeds the sapphire one for higher λ values. The effect of the environ-

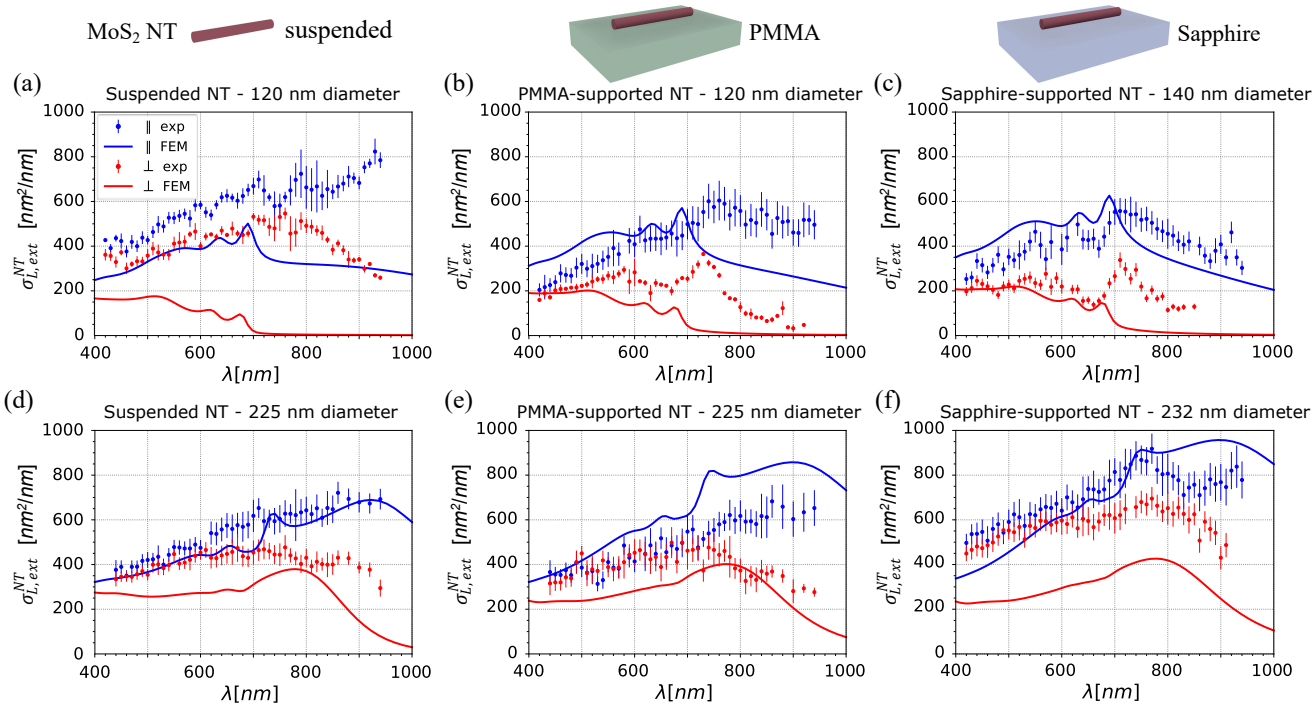

Figure 3: $\sigma^{NT}_{L,ext}$ vs λ for the suspended (a,d), PMMA-supported (b,e), and Al_2O_3-supported NT (c,f). Panels in first and second rows report data for small and wide diameter NTs, respectively. Light polarization parallel (blue) and perpendicular (red) to the NT axis: experimental (dots) and numerical (full lines) values. Reported sizes are from SEM imaging.

ment is even more pronounced for perpendicular polarization, where the relative difference of $\sigma^{NT}_{L,ext}$ among the suspended and supported NT cases is indeed greater at all wavelengths. For ease of visual comparison, the plots for different environments are reported on the same graphs for both parallel (Figure S3a) and perpendicular polarization (Figure S3c), respectively.

Features are best resolved for the suspended NT case, enabling the detection of a richer set of resonances, followed by the sapphire supported NT, and lastly by the PMMA supported one. With reference to Figure3a, the resonances at 650-660 nm, 590-600 nm and 450 nm are reminiscent of MoS_2 A (660 nm), B (602 nm) and C (459) bulk excitons, respectively.[2,22–24]

The features in the PMMA supported NT are a subset of those of the suspended one. The only exception is the resonance at 750 nm in parallel polarization (730 nm in perpendicular polarization) which, for the suspended case, is split in two resonances at 710 and 790 nm, respectively. The case of the sapphire supported NT exhibits a distinct although shallow resonance at 550 nm visible in parallel polarization (540 nm in perpendicular polarization) as compared to the case of the suspended NT.

Large diameters: D∼225 nm case. At variance with the D=120 nm case, $\sigma^{NT}_{L,ext}$ is greatest for the sapphire supported NTs over the entire wavelength range for both polarizations, the values for the suspended and PMMA supported NT being substantially similar throughout. For ease of visual comparison, the plots for different environments are reported on the same graphs for both parallel (Figure S3b) and perpendicular polarization (Figure S3d), respectively.

In general, spectral features for D∼225 nm are washed out with respect to the D∼120 nm case. For suspended NTs, $\sigma^{NT}_{L,ext}$ has comparable values throughout the wavelength range for both dimensions of the NTs. The optical response varies with NT diameters for the case of substrate-supported NTs. Specifically, for the case of the PMMA-supported NT, $\sigma^{NT}_{L,ext}$ values for D∼225 nm are slightly superior to the D∼120 nm case for parallel polarization, the difference becoming seizable for perpendicular

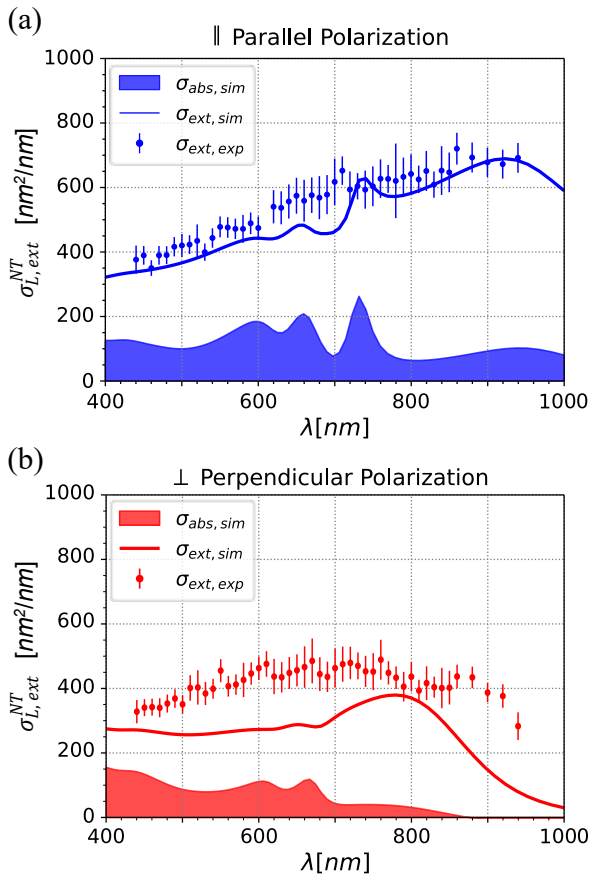

Figure 4: Absorption contribution to $\sigma^{NT}_{L,ext}$. Simulated $\sigma^{NT}_{L,ext}$ (full line) and $\sigma^{NT}_{L,abs}$ (shaded area) vs λ, for longitudinal (panel (a)) and perpendicular (panel (b)) polarization. Experimental data (full dots) are superposed for ease of comparison. Data are for the suspended NT, $D = 225$ nm case.

polarization. The difference in $\sigma^{NT}_{L,ext}$ between NTs of wide and small diameters is further enhanced in sapphire-supported NTs, where $\sigma^{NT}_{L,ext}$ for $D{\sim}225$ nm significantly exceeds the value for $D{\sim}120$ nm, the difference increasing for longer wavelengths.

Numerical assessment of $\sigma^{NT}_{L,ext}$. We proceed to investigate, via FEM, the predictability of the measured results and the role of the parameter at stake in their determination.

The FEM model, further detailed in SI, accounts for the N.A. of the output objective, thus mimicking the actual experimental measurement. Simulation key inputs, for computing the NT optical response, consist of the NT geometry and dielectric function. The NT is mimicked as a hollow cylinder of external and internal diameters D and D_{in}, respectively. All FEM simulations are performed adopting, for large NTs, $D_{in} = 190$ nm and $D = 230$ nm, while, for small NTs, D_{in}=120nm and D=140 nm. The values adopted for D are close to the values observed in SEM images, while the choices for D_{in} imply wall thicknesses of 20 and 10 nm for large and small NTs, respectively, that is values compatible with results from Raman spectra.

We take the anisotropic bulk MoS_2 dielectric tensor from Ermolaev et al. works.[25,26] Specifically these enable accounting for the different dielectric functions for the in-plane[25] and out-of-plane directions.[26] The bulk dielectric tensor is then modified to account for the roll-up of the MoS_2 layer to obtain the NT. The impact of different available optical constants tables for MoS_2 on the calculated $\sigma^{NT}_{L,ext}$ values are reported in Figure S6a.

Simulation results are reported in Figure 3. They capture the order of magnitude of σ^{NT}_{ext} and qualitatively reproduce the spectral response of the experimental data. For the case of perpendicular polarization, discrepancies are observed, particularly for the case of suspended $D = 120$ nm NT and sapphire-supported $D = 232$ nm NT. The agreement is less consistent at longer wavelengths. Nevertheless, the general agreement is noteworthy. Indeed, simulations suffer from uncertainties in the input parameters. Namely, the thickness of the measured NT walls remains uncertain. TEM images in Figure 1 show that the NT morphology deviates from that of an ideal tube. Furthermore, NTs are characterized by the exfoliation of the internal walls which bundle up and partially fill the empty space at the core. These findings indicate that the geometry of the adopted model and the dielectric function may require further refinement. To test for the former, we run simulations varying either the external (Figure S6c), internal diameter only (Figure S6d), or both but keeping the wall thickness unaltered (Figure S6b). The differences are sizable at long wavelengths, except for the case in which the wall thickness is kept constant. This suggests

that the uncertainty on the NT internal morphology, evidenced in Figure 1c, does play a role. Moreover, the accuracy of the dielectric function used in these calculations has some degree of uncertainty. The actual dielectric function is likely influenced by the specific NT morphology and actual MoS_2 planes orientation, which could be another reason for the differences in the numerical results.

FEM simulations allow to gain insight into the respective contributions of absorption, $\sigma^{NT}_{L,abs}$, and scattering, $\sigma^{NT}_{L,sca}$, cross sections per unit length to the overall $\sigma^{NT}_{L,ext}$. Notably, the diameters of the NTs are only slightly inferior to the laser wavelengths, which precludes the assumption that the extinction cross section is equivalent to the absorption one. We pin-point that the present situation is at variance with the paradigmatic case of individual single wall CNTs,[27–29] where $D \ll \lambda$ and the extinction cross section is solely due to absorption. Based on Mie theory, we intuitively expect the D=225 nm case to be most affected by scattering. We therefore focus on the case of the suspended D= 225 nm NT. Figure 4 reports the contribution of the simulated absorption cross section per unit length $\sigma^{NT}_{L,abs}$ (shaded area) to $\sigma^{NT}_{L,ext}$ (full line). The measured extinction cross section per unit length is also reported on the same graph. The scattering cross section per unit length, $\sigma^{NT}_{L,sca} = \sigma^{NT}_{L,ext} - \sigma^{NT}_{L,abs}$, contributes similarly to $\sigma^{NT}_{L,abs}$ for λ values in the 400-450 nm range, becoming the leading term as λ increases, particularly beyond 700 nm. A similar behaviour is observed also for the case of D = 120 nm, although with a less pronounced predominance of σ^{NT}_{sca} over σ^{NT}_{abs} for wavelengths short of 700 nm. Comparison of panels (a) and (b) shows that parallel polarization enhances scattering up to $\sim$ 900 nm, whereas it drops off beyond $\sim$ 760 nm in perpendicular polarization.

At first, it may seem surprising that absorption occurs at wavelengths above 700 nm, but a closer look reveals that it's actually expected. Indeed, the imaginary part of the dielectric function k drops significantly at 700 nm (at 700 nm it falls to one tenth of its value at 600 nm), consistent with the fact that, in the case of bulk MoS_2, the gap is expected to occur around 700 nm wavelengths (1.77 eV). Nevertheless, k is not strictly null for $\lambda > 700$ nm[25,26] and, when combined with geometric effects, it still leads to noticeable absorption. In essence, for wavelengths below 700 nm, the dielectric constant is the main driver of absorption, while above 700 nm, geometric effects take over resulting in Mie resonances, similarly to localized surface plasmon resonance.

Conclusions

In conclusion, we reported the *absolute* experimental values of the optical extinction cross section per unit length of *single* MoS_2 multi-wall NTs in the wavelength range spanning from 440 to 940 nm. Measuring individual NTs enabled us to correlate results with their specific dimensions, composition, and, to a certain extent, morphology, a crucial consideration given the wide dispersion of these properties.

Our measurements reveal a strong dependence on the diameter of the NT and its environment, with significant variations observed between suspended, sapphire-supported, and PMMA-supported configurations. The values are highly sensitive to the polarization of light, with distinct differences observed between parallel and perpendicular polarizations. Finite element simulations, informed by morphological input parameters from electron microscopies, indicated that both absorption and scattering contribute significantly to the extinction cross section per unit length, with the relative contributions varying depending on the NT diameter, surroundings and light polarization.

The present work is of relevance to a wide community. On the fundamental side, it provides benchmark values for theoretical investigations on the nanooptical response of a single MoS_2 NT. Under an applicative stand point, it will contribute to the rational design of MoS_2-based devices with tailored optical characteristics of potential interest in optoelectronics applications.

The present work identifies areas for future research to build upon the current understanding. Notably, the agreement between experi-

ment and simulation was only qualitatively satisfactory in some cases, highlighting the need for a more accurate dielectric function for realistic MoS_2 multiwall NTs. Along the same line, further improving NTs morphology would also enhance the agreement between experiment and simulations.

Acknowledgement We aknowledge support from the French National Research Agency (ANR-20-CE30-0016 ULTRASINGLE project), Université de Lyon (IDEXLYON-IMPULSION program), the European Union's HORIZON EUROPE framework program for research and innovation (grant agreement n. 101094299 "IMPRESS"), Ministero dell'Università e della Ricerca (PRIN Project No. 2022249HSF AITEM). L.M. and F.R acknowledge the National Recovery and Resilience Plan (NRRP), Mission 04 Component 2 Investment 1.5 – NextGenerationEU, Call for tender n. 3277 dated 30/12/2021. Award Number: 0001052 dated 23/06/2022. F.R. acknowledges the INFN project MANIFOLD.

Supporting Information Available

Supporting Information (SI) entails the following sections:

1. Experimental setup.
2. Simulated output signal.
3. Effects of polarization, environment and diameters.
4. FEM simulations details.
5. FEM: effects of dielectric constants and morphology.

References

(1) Yadgarov, L.; Tenne, R. Nanotubes from Transition Metal Dichalcogenides: Recent Progress in the Synthesis, Characterization and Electrooptical Properties. *Small* **2024**, 2400503.

(2) Sinha, S. S.; Yadgarov, L.; Aliev, S. B.; Feldman, Y.; Pinkas, I.; Chithaiah, P.; Ghosh, S.; Idelevich, A.; Zak, A.; Tenne, R. MoS2 and WS2 nanotubes: Synthesis, structural elucidation, and optical characterization. *The Journal of Physical Chemistry C* **2021**, *125*, 6324–6340.

(3) Pelella, A.; Kumar, A.; Intonti, K.; Durante, O.; De Stefano, S.; Han, X.; Li, Z.; Guo, Y.; Giubileo, F.; Camilli, L.; others WS2 Nanotube Transistor for Photodetection and Optoelectronic Memory Applications. *Small* **2024**, 2403965.

(4) Aftab, S.; Iqbal, M. Z.; Rim, Y. S. Recent advances in rolling 2D TMDs nanosheets into 1D TMDs nanotubes/nanoscrolls. *Small* **2023**, *19*, 2205418.

(5) Zhang, C.; Wang, S.; Yang, L.; Liu, Y.; Xu, T.; Ning, Z.; Zak, A.; Zhang, Z.; Tenne, R.; Chen, Q. High-performance photodetectors for visible and near-infrared lights based on individual WS2 nanotubes. *Applied physics letters* **2012**, *100*.

(6) Strojnik, M.; Kovic, A.; Mrzel, A.; Buh, J.; Strle, J.; Mihailovic, D. MoS2 nanotube field effect transistors. *AIP Advances* **2014**, *4*.

(7) Fathipour, S.; Remskar, M.; Varlec, A.; Ajoy, A.; Yan, R.; Vishwanath, S.; Rouvimov, S.; Hwang, W.; Xing, H.; Jena, D.; others Synthesized multiwall MoS2 nanotube and nanoribbon field-effect transistors. *Applied Physics Letters* **2015**, *106*.

(8) Shiraiwa, N.; Murata, K.; Nakazawa, T.; Fukawa, A.; Takase, K.; Ito, T.; Shingubara, S.; Shimizu, T. Fabrication and characterization of field-effect transistors based on MoS2 nanotubes prepared in anodic aluminum oxide templates. *Micro and Nano Engineering* **2023**, *19*, 100200.

(9) Kazanov, D.; Poshakinskiy, A.; Davydov, V. Y.; Smirnov, A.; Eliseyev, I.; Kirilenko, D.; Remškar, M.; Fathipour, S.;

Mintairov, A.; Seabaugh, A.; others Multiwall MoS2 tubes as optical resonators. *Applied Physics Letters* **2018**, *113*.

(10) Kazanov, D.; Rakhlin, M.; Poshakinskiy, A.; Shubina, T. Towards exciton-polaritons in an individual MoS2 nanotube. *Nanomaterials* **2020**, *10*, 373.

(11) Galimov, A.; Kazanov, D.; Poshakinskiy, A.; Rakhlin, M.; Eliseyev, I.; Toropov, A.; Remškar, M.; Shubina, T. Direct observation of split-mode exciton-polaritons in a single MoS 2 nanotube. *Nanoscale Horizons* **2024**,

(12) Eliseyev, I. A.; Borodin, B. R.; Kazanov, D. R.; Poshakinskiy, A. V.; Remškar, M.; Pavlov, S. I.; Kotova, L. V.; Alekseev, P. A.; Platonov, A. V.; Davydov, V. Y.; others Twisted nanotubes of transition metal dichalcogenides with split optical modes for tunable radiated light resonators. *Advanced Optical Materials* **2023**, *11*, 2202782.

(13) Qian, Q.; Zu, R.; Ji, Q.; Jung, G. S.; Zhang, K.; Zhang, Y.; Buehler, M. J.; Kong, J.; Gopalan, V.; Huang, S. Chirality-dependent second harmonic generation of MoS2 nanoscroll with enhanced efficiency. *ACS nano* **2020**, *14*, 13333–13342.

(14) Feldman, Y.; Wasserman, E.; Srolovitz, D.; Tenne, R. High-rate, gas-phase growth of MoS2 nested inorganic fullerenes and nanotubes. *Science* **1995**, *267*, 222–225.

(15) Remškar, M. Inorganic nanotubes. *Advanced Materials* **2004**, *16*, 1497–1504.

(16) Chithaiah, P.; Ghosh, S.; Idelevich, A.; Rovinsky, L.; Livneh, T.; Zak, A. Solving the "MoS2 nanotubes" synthetic enigma and elucidating the route for their catalyst-free and scalable production. *ACS nano* **2020**, *14*, 3004–3016.

(17) Lee, C.; Yan, H.; Brus, L. E.; Heinz, T. F.; Hone, J.; Ryu, S. Anomalous lattice vibrations of single-and few-layer MoS2. *ACS nano* **2010**, *4*, 2695–2700.

(18) Reddy, R. K. K.; Kailasa, S.; Rani, B. G.; Jayarambabu, N.; Yasuhiko, H.; Ramana, G. V.; Rao, K. V. Hydrothermal approached 1-D molybdenum oxide nanostructures for high-performance supercapacitor application. *SN Applied Sciences* **2019**, *1*, 1–9.

(19) He, Z.; Zhao, R.; Chen, X.; Chen, H.; Zhu, Y.; Su, H.; Huang, S.; Xue, J.; Dai, J.; Cheng, S.; others Defect engineering in single-layer MoS2 using heavy ion irradiation. *ACS applied materials & interfaces* **2018**, *10*, 42524–42533.

(20) Mignuzzi, S.; Pollard, A. J.; Bonini, N.; Brennan, B.; Gilmore, I. S.; Pimenta, M. A.; Richards, D.; Roy, D. Effect of disorder on Raman scattering of single-layer Mo S 2. *Physical Review B* **2015**, *91*, 195411.

(21) Crut, A.; Maioli, P.; Del Fatti, N.; Vallée, F. Optical absorption and scattering spectroscopies of single nano-objects. *Chemical Society Reviews* **2014**, *43*, 3921–3956.

(22) Wilson, J. A.; Yoffe, A. The transition metal dichalcogenides discussion and interpretation of the observed optical, electrical and structural properties. *Advances in Physics* **1969**, *18*, 193–335.

(23) Acrivos, J. V.; Liang, Y.; Wilson, J.; Yoffe, A. Optical studies of metal-semiconductor transmutations produced by intercalation. *Journal of Physics C: Solid State Physics* **1971**, *4*, L18.

(24) Munkhbat, B.; Baranov, D. G.; Stührenberg, M.; Wersäll, M.; Bisht, A.; Shegai, T. Self-hybridized exciton-polaritons in multilayers of transition metal dichalcogenides for efficient light absorption. *Acs Photonics* **2018**, *6*, 139–147.

(25) Ermolaev, G. A.; Stebunov, Y. V.; Vyshnevyy, A. A.; Tatarkin, D. E.; Yakubovsky, D. I.; Novikov, S. M.; Baranov, D. G.; Shegai, T.; Nikitin, A. Y.; Arsenin, A. V.; others Broadband optical properties of monolayer and bulk MoS2. *npj 2D Materials and Applications* **2020**, *4*, 21.

(26) Ermolaev, G.; Grudinin, D.; Stebunov, Y.; Voronin, K. V.; Kravets, V.; Duan, J.; Mazitov, A.; Tselikov, G.; Bylinkin, A.; Yakubovsky, D.; others Giant optical anisotropy in transition metal dichalcogenides for next-generation photonics. *Nature communications* **2021**, *12*, 854.

(27) Blancon, J.-C.; Paillet, M.; Tran, H. N.; Than, X. T.; Guebrou, S. A.; Ayari, A.; Miguel, A. S.; Phan, N.-M.; Zahab, A.-A.; Sauvajol, J.-L.; others Direct measurement of the absolute absorption spectrum of individual semiconducting single-wall carbon nanotubes. *Nature communications* **2013**, *4*, 2542.

(28) Christofilos, D.; Blancon, J.-C.; Arvanitidis, J.; Miguel, A. S.; Ayari, A.; Del Fatti, N.; Vallée, F. Optical imaging and absolute absorption cross section measurement of individual nano-objects on opaque substrates: single-wall carbon nanotubes on silicon. *The Journal of Physical Chemistry Letters* **2012**, *3*, 1176–1181.

(29) Vialla, F.; Malic, E.; Langlois, B.; Chassagneux, Y.; Diederichs, C.; Deleporte, E.; Roussignol, P.; Lauret, J.-S.; Voisin, C. Universal nonresonant absorption in carbon nanotubes. *Physical Review B* **2014**, *90*, 155401.

TOC Graphic

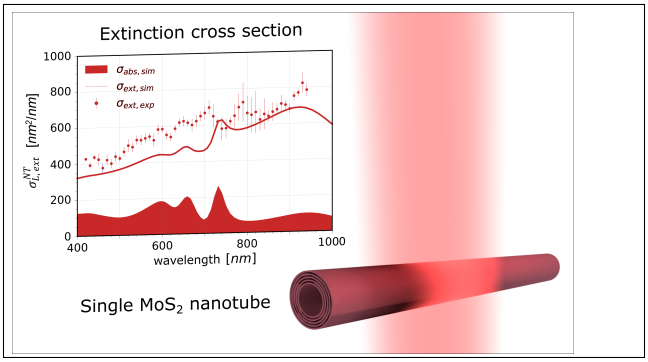
Extinction cross section
1000
800
600
400
200
0
400
600
800
1000
wavelength [nm]
$\sigma_{abs,sim}$
$\sigma_{ext,sim}$
$\sigma_{ext,exp}$
$\sigma^{NT}_{L,ext}$ [nm²/nm]
Single MoS2 nanotube